Observation of Nonlocal Heat Flux Using Thomson Scattering

In diverse fields of plasma physics including astrophysics, inertial confinement fusion, and magnetohydrodynamics, classical thermal transport[1,2] provides the foundation for calculating heat flux.[3–7] The classical theories of thermal transport by Spitzer–Härm (SH)[1] and Braginskii[2] specify the heat flux by a local expression in terms of the thermal conductivity κ and the electron temperature gradient (e.g., $\mathbf{q}_{SH} = \kappa \nabla T_e$). This theory breaks down in the presence of large temperature gradients,[8–11] turbulence,[12] or return current instabilities:[13–16] classical theory does not include nonlocal effects where energetic electrons travel distances comparable with the temperature scale length before colliding.

Local thermal-transport theories[1,2] follow from a perturbative solution of a kinetic equation in terms of the collision parameter $\lambda_{ei}/L_T \ll 1$, where λ_{ei} is the electron–ion (e–i) mean free path and $L_T = |\nabla \ln(T_e)|^{-1}$ is the scale length of the temperature gradient. Nonlocal theories overcome limitations of classical theory by accounting for the range of electron–ion mean free paths associated with different electron velocities. By extending closure relations for hydrodynamic models into the kinetic regime of weak collisions, these theories[17–24] have established the limits of classical transport $\left(\lambda_{ei}/L_T \sim 10^{-2}\right)$.

In laser-produced plasmas, classical theory predicts unphysically large thermal transport. Hydrodynamic simulations of these plasmas require an *ad hoc* limiter on the heat flux to match experimental observables. Historically these limiters were set by kinetic simulations,[25–27] integrated experiments,[10,11,28,29] or more-focused Thomson-scattering measurements of the local plasma conditions (i.e., electron temperature and density).[8,13,30,31] More recently, the nonlocal Schurtz–Nicolaï–Busquet (SNB) model[23] was introduced as a computationally efficient method for calculating the nonlocal heat flux in large-scale multidimensional hydrodynamic simulations. Experiments that attempt to measure nonlocal transport have been limited, however, to indirect observations.[8,24,30–32]

In this article, we present the first direct measurement of nonlocal heat flux. A novel implementation of collective Thomson scattering measured the heat flux by probing the relative spectral amplitudes of electron plasma waves (Fig. 155.1). In addition to the heat flux, the plasma-wave spectrum provided a measurement of the plasma temperature and density profiles. The profiles were used to calculate the classical SH heat flux, which was in good agreement with the measured heat flux far from the target, where the temperature scale length was
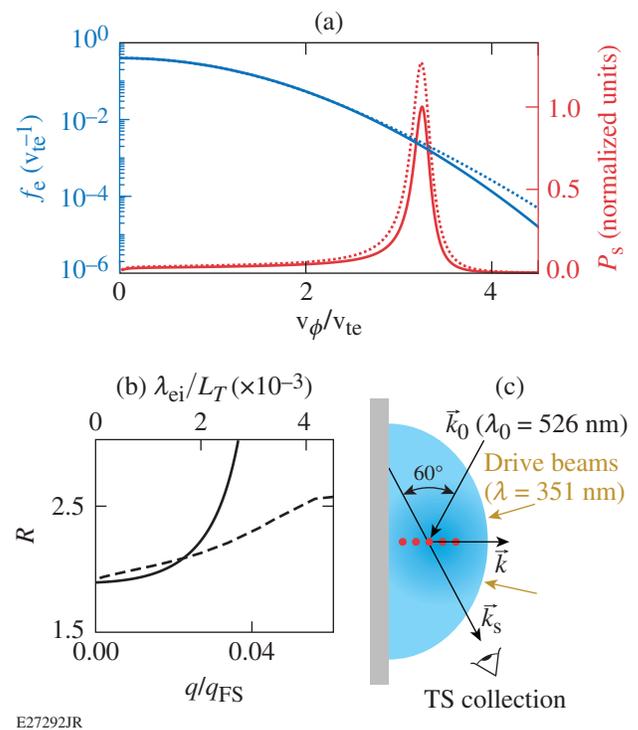
Figure 155.1

(a) Calculated Thomson-scattering (TS) features (red curves, right axis) from electron plasma waves [Eq. (1)] are shown ($v_\phi = \omega/k$) using a Maxwellian (solid blue curve, left axis) electron distribution function and the non-Maxwellian (dotted blue curve) distribution that accounts for classical Spitzer–Härm (SH) heat flux $\left(\lambda_{ei}/L_T = 2.2 \times 10^{-3}, q/q_{FS} = 3\%\right)$. (b) For a fixed normalized phase velocity, the ratio (R) of the peak scattered power of the up- and downshifted features are shown for calculations that use classical SH (solid curve, top axis) and nonlocal (dashed curve, bottom axis) distribution functions over a range of heat flux normalized to the free-streaming flux, $q_{FS} = n_e T_e v_{te}$. (c) Schematic of the setup.

E27292JR

longer than the electron–ion mean free path of heat-carrying electrons $\left(\lambda_{ei}/L_T \sim 10^{-3}\right)$. For steeper gradients, the measured heat flux was up to a factor of 2 smaller than the classical values as a result of nonlocal transport. For the most nonlocal conditions, the SNB model predicted an inhibited heat flux compared with the classical values, but it still overestimated the measured heat flux by ~40%. In the region where classical SH theory agrees with the measured heat flux, the SNB model overestimates the flux.

Figure 155.1(a) illustrates the effect of heat flux on the collective Thomson-scattering spectrum. Two scattering spectra, calculated with and without SH heat flux, demonstrate the sensitivity of the Thomson-scattering spectrum to the shape of the electron distribution function. The SH distribution function was derived from the lowest-order terms in the perturbative solution of the kinetic equation, $f_{SH} = (\mathbf{v}) = f_0^M(\mathbf{v}) + \cos\theta f(\mathbf{v})$, where

$$f(\mathbf{v}) = \lambda_{ei}/L_T \sqrt{2/9\pi} \left(\mathbf{v}/v_{te}\right)^4 \left(4 - \mathbf{v}^2/2v_{te}^2\right) f_0^M(\mathbf{v}),$$

$v_{te} = \sqrt{T_e/m_e}$ is the electron thermal velocity, f_0^M is a Maxwellian velocity distribution function, and θ is the angle between electron velocity and the temperature gradient. The Thomson-scattering spectra were calculated in the high-frequency limit where the ion dynamics can be ignored:[33]

$$S(\mathbf{k},\omega) = \frac{2\pi}{k} \frac{\tilde{f}_e(\omega/k)}{\left|\varepsilon(\mathbf{k},\omega)\right|^2}, \qquad (1)$$

where $\varepsilon(\mathbf{k},\omega)$ is the longitudinal plasma dielectric function and the probed wave vector (frequency) is the difference between the incident and scattered wave vectors (frequencies), $\mathbf{k} = \mathbf{k}_i - \mathbf{k}_s(\omega = \omega_i - \omega_s)$. The 1-D distribution function $\tilde{f}_e(v)$ is determined by integrating the full distribution function over velocities perpendicular to the probed wave vector. At the Langmuir wave resonance defined by $\varepsilon(\mathbf{k},\omega) = 0$, $\omega(k) = \pm\omega_L(k) + i\gamma_L(k)$, where, in general, the Landau damping rate γ_L is proportional to

$$\partial\tilde{f}_e/\partial v\big|_{v=\omega_L/k}$$

and ω_L is approximately the resonant frequency for Langmuir fluctuations. The collisionless approximation of $S(\mathbf{k},\omega)$ in Eq. (1) is valid for these experiments beceuase the scale of the probed waves (~1/k) is small compared to the electron–ion mean free path such that $k\lambda_{ei} \gg 1$.

Figure 155.1(b) shows the sensitivity of the amplitude ratio of the up- and downshifted (red- and blue-shifted, respectively) scattered peaks to heat flux, where SH or nonlocal distribution functions were used to calculate the Thomson-scattering spectrum. It is evident from Eq. (1) that heat flux has two effects on the scattered power near the resonance: (1) the amplitude depends on the number of electrons at the resonance $\left[\tilde{f}_e(\omega_L/k)\right]$ and (2) the width is given by the slope of the electron distribution function at the resonance

$$\partial\tilde{f}_e/\partial v\big|_{v=\omega_L/k}.$$

Therefore, to maximize the effect of heat flux on the scattered power, the scattering geometry was chosen to probe Langmuir waves propagating along the target normal where the temperature is largest, $\mathbf{k} \parallel -\nabla T_e$, and with phase velocities near the region of the electron distribution function with the most heat-carrying electrons, $\omega_L/k \gtrsim 3.4v_{te}$. For this geometry, it was demonstrated in theory[34] that the Langmuir fluctuations that contribute to the red-shifted peak in the Thomson-scattering spectrum experience increased Landau damping, while the oppositely propagating Langmuir waves that contribute to blue-shifted peak become less damped.

The experiment was conducted on LLE's OMEGA laser[35] and used six $\lambda_{3\omega} = 351$-nm beams to produce a blowoff plasma from a planar aluminum target. Each beam had 250 J in a 2-ns flattop pulse. Phase plates[36] were used to set the profile of the laser spot at the target plane to be a high-order super-Gaussian ($n = 4.6$) with a full width at half maximum of 560 μm. The six beams with the smallest angle of incidence (8°, 29°, 32°, 33°, 35°, and 40°) were chosen to produce the plasma [Fig. 155.1(c)]. The Thomson-scattering diagnostic[37] consisted of a 40-J, 2-ns-long, $\lambda_{2\omega} = 526.5$-nm probe beam with a best-focus diameter of ~50 μm (Ref. 38). The light scattered from a 50-μm × 50-μm × 50-μm volume was imaged through a 1/3-m spectrometer onto a streak camera. The spectral dispersion was 0.411 nm/pixel±0.4%. The system had spectral and temporal resolutions of 0.5 nm±5% and 20 ps±0.5%, respectively. The scattering angle was 60°. The scattering volume was set to five different locations along the target normal ranging from 1.1 mm to 1.5 mm from the initial target surface. To account for the bremsstrahlung radiation collected by the Thomson-scattering system, a background was established at each location by turning off the Thomson-scattering probe beam and was subtracted from the corresponding spectrum.

Figure 155.2 shows the collective Thomson-scattering spectra measured at each of the probed locations. The data were
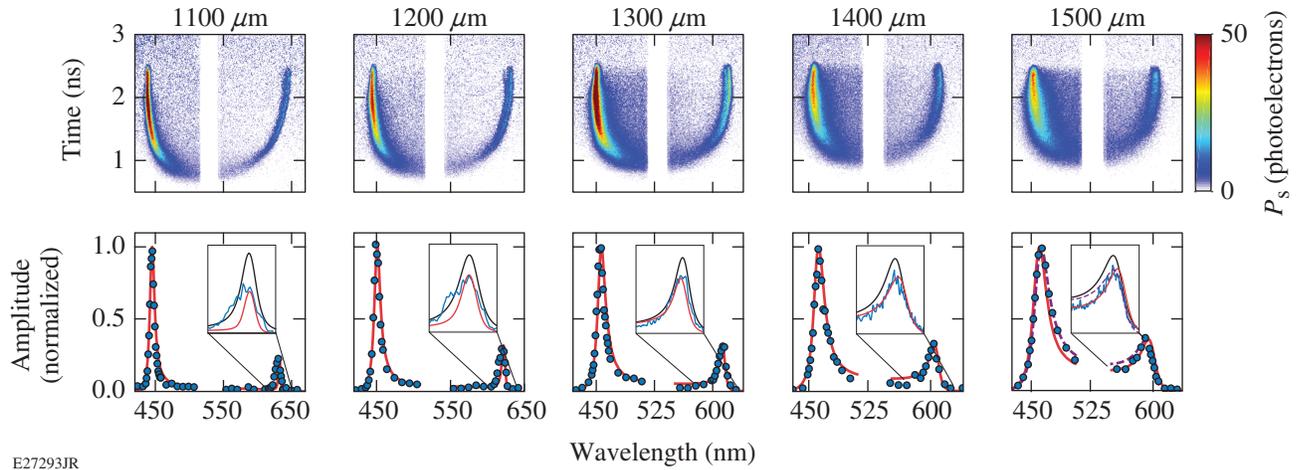
Figure 155.2
The measured collective Thomson-scattering spectra (top row) and the corresponding spectral profiles (blue dots) at 1.5 ns (bottom row). The data were fit (red) with Eq. (1) using non-Maxwellian electron distribution functions to measure heat flux. (Insets) The red-shifted features are shown with calculations (black) that used the plasma conditions from the fit but a Maxwellian electron distribution function. These spectra recover the location of the scattering features but fail to match their amplitudes. At 1.5 mm, the spectrum was fit (dashed curve) with calculations that use a distribution function consistent with classical SH theory. All spectra are normalized to the peak scattered power.

fit with a fully kinetic Thomson-scattered power spectrum[33] that incorporates a non-Maxwellian electron distribution function to provide a measure of the heat flux, electron temperature, and density.[34] To a good approximation, the relative amplitudes of the electron plasma wave features are given by heat flux, the frequency of the electron plasma wave feature by the density, and the width of the plasma wave feature by the electron temperature.

The insets in Fig. 155.2 compare scattered spectra calculated using non-Maxwellian electron distribution functions, consistent with thermal transport, with Maxwellian electron distribution functions. The excellent quality of the fits over the complete spectrum indicates the high accuracy of the shape of the distribution functions used. The significant deviation from the measured spectra that occurs when not accounting for the effects of heat flux (i.e., Maxwellian distribution functions) shows the sensitivity of the measurement. The non-Maxwellian distribution functions were calculated from a series of Fokker–Planck simulations[39] with varying boundary conditions but with the electron temperature and density profiles equal to the measured values.

Figure 155.3 shows the resulting heat-flux measurements at the five probed locations obtained by integrating the electron distribution functions used to fit the Thomson-scattering spectrum $\left[\mathbf{q}_{TS} = \int (1/2) m v^2 \mathbf{v} f_e(\mathbf{v}) d^3 v \right]$. The measured heat flux is compared to classical heat flux values ($\mathbf{q}_{SH} = -\kappa \nabla T_e$) determined by calculating the Spitzer thermal conductiv-
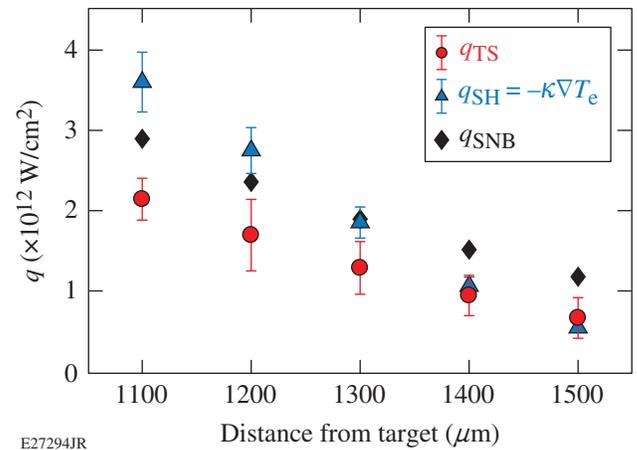
Figure 155.3
The heat flux (red circles) measured along the target normal is compared with classical heat flux (SH) calculations (blue triangles) and heat-flux values obtained from the simulations using the Schurtz–Nicolaï–Busquet (SNB) model (black diamonds). Both the simulations and calculations were initiated with the measured electron temperatures and densities. For reference, $\lambda_{ei}/L_T = 1.4 \times 10^{-2}, 1.4 \times 10^{-2}, 1.3 \times 10^{-2}, 1.0 \times 10^{-2}$, and 7×10^{-3} at 1.1 mm, 1.2 mm, 1.3 mm, 1.4 mm, and 1.5 mm, respectively.

ity and the local temperature gradient from the measured plasma profiles (Fig. 155.4). Excellent agreement between the classical and measured heat flux is observed for the location farthest from the target surface, but for locations closer to the target surface, the measured flux is smaller than the classical values. This difference highlights the nonlocal nature of the thermal transport.

E27295JR
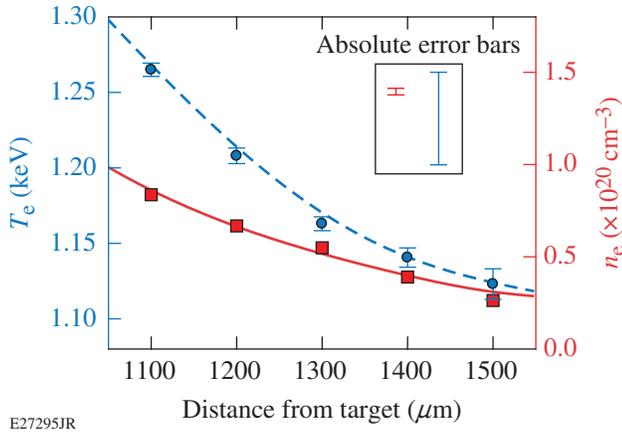
Figure 155.4

Electron temperature (blue circles, left axis) and density (red squares, right axis) measurements at $t = 1.5$ ns. Profiles of electron temperature (dashed blue curve) and density (solid red curve) used in Fokker–Planck simulations. The relative (1σ statistical) error bars are shown with the temperature measurements. The absolute error bars are represented in the inset.

Figure 155.4 presents the measured electron temperature and density profiles determined from fitting the blue-shifted features with the Thomson-scattering power spectrum, assuming Maxwellian electron distribution functions (Fig. 155.2). The electron temperature decreased from 1.27 ± 0.04 keV to 1.12 ± 0.04 keV over 400 μm. The electron temperature gradient at each measurement location was determined by fitting a fifth-order polynomial to the measurements. The uncertainty in the temperature gradient was calculated by varying the data within the relative error bars, which were used to calculate the errors in the classical heat flux (Fig. 155.3). Over this same distance, the electron density dropped from $8.36 \pm 0.04 \times 10^{19}$ cm^{-3} to $2.63 \pm 0.01 \times 10^{19}$ cm^{-3}. The high signal-to-noise ratio in the measured spectra resulted in excellent χ^2 statistical fits, which determined the 1σ statistical relative error bars shown in Fig. 155.4. The absolute errors in the electron temperature and density were dominated by uncertainties in the spectral dispersion and resolution. Adding these errors in quadrature resulted in a 2% and 3% absolute error in the density and temperature, respectively.

For the measurement farthest from the target surface (1.5 mm), the Thomson-scattering spectrum calculated using the electron distribution function determined by classical SH theory, where $\lambda_{ei}/L_T = 7 \times 10^{-3}$, was in good agreement (Fig. 155.2). This is consistent with the agreement in the measured heat flux at this location presented in Fig. 155.3. Although the classical SH distribution function allows the amplitudes of the spectral peaks to be reproduced, the fit shows a discrepancy

in the width of the red-shifted peak, suggesting that the shape of the SH electron distribution function around the resonance is incorrect. For locations closer to the target, the electron distribution function predicted by classical theory becomes negative at velocities around the Langmuir wave resonances, and classical theory cannot be used to fit the measured spectrum. This is consistent with the measured heat flux being significantly less than the classical values (Fig. 155.3). At these locations $\lambda_{ei}/L_T > 10^{-3}$, which confirms experimentally the limit of validity previously determined by nonlocal theories.[17–22]

To determine the electron distribution functions consistent with nonlocal transport, the K2 Vlasov–Fokker–Planck code[39] was used. K2 uses a Legendre polynomial representation of the electron distribution function, $f(t,x,\mathbf{v}) = \sum_n f_n(t,x,v)P_n(\theta)$, where x is the direction along the target normal. K2 solves for the self-consistent electric field and includes the effects of electron–ion scattering and electron–electron collisions. To capture the fine detail in the distribution functions at high velocities, close to the Langmuir wave resonances, polynomials up to and including f_8 were required. In all calculations, the plasma profiles were initially set to the measurements (Fig. 155.4) and the temperature at the boundary of the simulation closest to the target (~500 μm) was varied between 1.2 keV and 2 keV. Since the transport is nonlocal, the choice of boundary condition is important to determine heat flow at the edge of the measurement region (i.e., 1.1 mm) but has a small effect at the other measurement positions.

Once the initial conditions were set, the K2 code evolved the distribution function in time and, after a few collision times, reached steady state. Over this time, a small amount of heating/cooling was applied to the electrons to help maintain the temperature profile close to the measured (i.e., initial) values. This approximately accounted for the small amount of ongoing thermal compression/expansion in the coronal region. Since the hydrodynamic motion is slow compared to the electron thermal transport, it was ignored. For each boundary condition, the electron distribution functions at each measurement position were used to calculate Thomson-scattering spectra. The boundary condition (1.8 keV) that generated the Thomson-scattering spectra with the best match across all locations was used to determine the measured heat flux. The resulting electron distribution functions were used in Eq. (1) to calculate the spectra shown in Fig. 155.2.

The measured heat flux was compared to calculations that used the multigroup nonlocal SNB model (Fig. 155.3), initialized with the measured electron temperature and density

profiles (Fig. 155.4). In the nonlocal region, where classical SH theory overestimates the flux, the SNB model calculates a flux that is about halfway between the classical and measured values. In the region where classical transport is valid (1.5 mm), the SNB model overestimates the flux by 75%. Furthermore, in the nonlocal transport regions, the electron distribution functions were negative around the electron plasma wave resonance, which made it impossible to fit the measured Thomson-scattering spectrum.

Figure 155.5 shows the flux contribution of electrons for each of the models at 1.2 mm from the target surface. According to the K2 model, the reduction in heat flux relative to the classical model at this location occurs as a result of a reduction in the flux of electrons with $v \gtrsim 3.4\ v_{te}$. Furthermore, the peak heat flow occurs at a lower velocity ($v_{K2} \approx 3.5\ v_{te}$) relative to the classical result ($v_{SH} \approx 3.7\ v_{te}$). The SNB model slightly inhibits the flux but still overpredicts the heat flow. The heat flux at this location is 60% of the classical value.
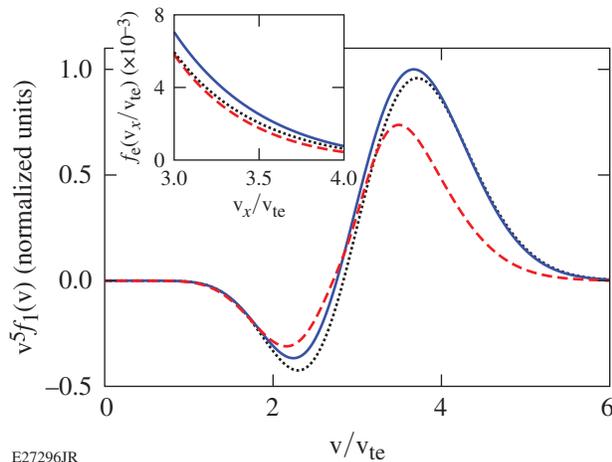
E27296JR

Figure 155.5
The velocity-dependent contribution of heat flux at 1200 μm for calculations using the Fokker–Planck (dashed red curve), classical (dotted blue curve), and SNB (solid black curve) models. The inset shows the corresponding electron distribution functions.

In summary, Thomson scattering was used to measure the heat flux directly from the amplitudes of the Langmuir fluctuations and indirectly through the electron temperature and density profiles ($q_{SH} = \kappa \nabla T_e$). The measured heat flux agreed with classical SH values when $\lambda_{ei}/L_T < 10^{-3}$, but in the opposite limit $\left(\lambda_{ei}/L_T > 10^{-3}\right)$, the differences were as large as a factor of 2. The multigroup nonlocal SNB model overpredicted the flux in all regions, which demonstrates the need to include

physics often missing from computationally expedient nonlocal models, most notably high-order polynomials for properly resolving velocity space, the self-consistent electric field, and a Fokker–Planck collision operator.

REFERENCES

1. L. Spitzer, Jr. and R. Härm, Phys. Rev. **89**, 977 (1953).

2. S. I. Braginskii, J. Exptl. Theoret. Phys. (U.S.S.R.) **33**, 459 (1957).

3. G. Zimmerman *et al.*, J. Opt. Soc. Am. **68**, 549 (1978).

4. M. M. Marinak *et al.*, Phys. Plasmas **3**, 2070 (1996).

5. B. Fryxell *et al.*, Astrophys. J. Suppl. Ser. **131**, 273 (2000).

6. A. J. Cunningham *et al.*, Astrophys. J. Suppl. Ser. **182**, 519 (2009).

7. B. Van der Holst *et al.*, Astrophys. J. Suppl. Ser. **194**, 23 (2011).

8. G. Gregori, S. H. Glenzer, J. Knight, C. Niemann, D. Price, D. H. Froula, M. J. Edwards, R. P. J. Town, A. Brantov, W. Rozmus, and V. Yu. Bychenkov, Phys. Rev. Lett. **92**, 205006 (2004).

9. R. D. Petrasso, J. A. Frenje, C. K. Li, F. H. Séguin, J. R. Rygg, B. E. Schwartz, S. Kurebayashi, P. B. Radha, C. Stoeckl, J. M. Soures, J. Delettrez, V. Yu. Glebov, D. D. Meyerhofer, and T. C. Sangster, Phys. Rev. Lett. **90**, 095002 (2003).

10. J. A. Tarvin *et al.*, Phys. Rev. Lett. **51**, 1355 (1983).

11. T. J. Goldsack *et al.*, Opt. Commun. **42**, 55 (1982).

12. B. B. Kadomtsev and O. P. Pogutse, in *Reviews of Plasma Physics*, edited by M. A. Leontovich (Consultants Bureau, New York, 1970), Vol. 5, Chap. 2, pp. 249–400.

13. M. S. White, J. D. Kilkenny, and A. E. Dangor, Phys. Rev. Lett. **35**, 524 (1975).

14. V. Yu. Bychenkov, V. P. Silin, and S. A. Uryupin, Phys. Rep. **164**, 119 (1988).

15. S. H. Glenzer *et al.*, Phys. Rev. Lett. **88**, 235002 (2002).

16. D. R. Gray and J. D. Kilkenny, Plasma Phys. **22**, 81 (1980).

17. A. R. Bell, R. G. Evans, and D. J. Nicholas, Phys. Rev. Lett. **46**, 243 (1981).

18. J. P. Matte and J. Virmont, Phys. Rev. Lett. **49**, 1936 (1982).

19. A. R. Bell, Phys. Fluids **26**, 279 (1983).

20. J. F. Luciani, P. Mora, and J. Virmont, Phys. Rev. Lett. **51**, 1664 (1983).

21. J. R. Albritton, E. A. Williams, and I. B. Bernstein, Phys. Rev. Lett. **57**, 1887 (1986).

22. V. Yu *et al*., Phys. Rev. Lett. **75**, 4405 (1995).

23. G. P. Schurtz, Ph. D. Nicolaï, and M. Busquet, Phys. Plasmas **7**, 4238 (2000).

24. V. N. Goncharov, O. V. Gotchev, E. Vianello, T. R. Boehly, J. P. Knauer, P. W. McKenty, P. B. Radha, S. P. Regan, T. C. Sangster, S. Skupsky, V. A. Smalyuk, R. Betti, R. L. McCrory, D. D. Meyerhofer, and C. Cherfils-Clérouin, Phys. Plasmas **13**, 012702 (2006).

25. R. C. Malone, R. L. McCrory, and R. L. Morse, Phys. Rev. Lett. **34**, 721 (1975).

26. G. Murtaza, A. M. Mirza, and M. S. Qaisar, Phys. Scr. **47**, 811 (1993).

27. J. R. Albritton, Phys. Rev. Lett. **50**, 2078 (1983).

28. D. T. Michel, A. K. Davis, V. N. Goncharov, T. C. Sangster, S. X. Hu, I. V. Igumenshchev, D. D. Meyerhofer, W. Seka, and D. H. Froula, Phys. Rev. Lett. **114**, 155002 (2015).

29. W. C. Mead, E. M. Campbell, W. L. Kruer, R. E. Turner, C. W. Hatcher, D. S. Bailey, P. H. Y. Lee, J. Foster, K. G. Tirsell, B. Pruett, N. C. Holmes, J. T. Trainor, G. L. Stradling, B. F. Lasinski, C. E. Max, and F. Ze, Phys. Fluids B **27**, 1301 (1984).

30. S. H. Glenzer *et al*., Phys. Rev. Lett. **82**, 97 (1999).

31. D. H. Froula, J. S. Ross, L. Divol, N. Meezan, A. J. MacKinnon, R. Wallace, and S. H. Glenzer, Phys. Plasmas **13**, 052704 (2006).

32. J. Hawreliak *et al*., J. Phys. B: At. Mol. Opt. Phys. **37**, 1541 (2004).

33. D. H. Froula, S. H. Glenzer, N. C. Luhmann, Jr., and J. Sheffield, *Plasma Scattering of Electromagnetic Radiation: Theory and Measurement Techniques*, 2nd ed. (Academic Press, Amsterdam, 2011).

34. W. Rozmus *et al*., Phys. Plasma **23**, 012707 (2016).)

35. T. R. Boehly, D. L. Brown, R. S. Craxton, R. L. Keck, J. P. Knauer, J. H. Kelly, T. J. Kessler, S. A. Kumpan, S. J. Loucks, S. A. Letzring, F. J. Marshall, R. L. McCrory, S. F. B. Morse, W. Seka, J. M. Soures, and C. P. Verdon, Opt. Commun. **133**, 495 (1997).

36. T. J. Kessler, Y. Lin, J. J. Armstrong, and B. Velazquez, Proc. SPIE **1870**, 95 (1993).

37. J. Katz, R. Boni, C. Sorce, R. Follett, M. J. Shoup III, and D. H. Froula, Rev. Sci. Instrum. **83**, 10E349 (2012).

38. A. J. Mackinnon, S. Shiromizu, G. Antonini, J. Auerbach, K. Haney, D. H. Froula, J. Moody, G. Gregori, C. Constantin, C. Sorce, L. Divol, R. L. Griffith, S. Glenzer, J. Satariano, P. K. Whitman, S. N. Locke, E. L. Miller, R. Huff, K. Thorp, W. Armstrong, W. Bahr, W. Seka, G. Pien, J. Mathers, S. Morse, S. Loucks, and S. Stagnitto, Rev. Sci. Instrum. **75**, 3906 (2004).

39. M. Sherlock, J. P. Brodrick, and C. P. Ridgers, Phys. Plasmas **24**, 082706 (2017).